Novel ZnO/Ag nanohybrids prepared from Ag+-doped layered zinc hydroxides as highly active photocatalysts for the degradation of dyes and Ciprofloxacin

Mouna Ibn Mahrsi, Bilel Chouchene, Thomas Gries, Vincent Carré, Emilien Girot, Ghouti Medjahdi, Fadila Ayari, Balan Lavinia, Raphaël Schneider

Novel ZnO/Ag nanohybrids prepared from Ag^+-doped layered zinc hydroxides as highly active photocatalysts for the degradation of dyes and Ciprofloxacin

Mouna Ibn Mahrsi,[a,b] Bilel Chouchene,[a] Thomas Gries,[c] Vincent Carré,[d] Emilien Girot,[a] Ghouti Medjahdi,[c] Fadila Ayari,[b] Lavinia Balan,[e] Raphaël Schneider [a*]

[a] Université de Lorraine, CNRS, LRGP, F-54000 Nancy, France

[b] Carthage University, Faculty of Sciences of Bizerte, LR 05/ES09 Laboratory of Applications of Chemistry to Resources and Natural Substances and to the Environment (LACReSNE), Zarzouna 7021, Tunisia

[c] Université de Lorraine, CNRS, IJL, F-54000 Nancy, France

[d] Université de Lorraine, LCP-A2MC, F-57000 Metz, France

[e] CEMHTI-UPR 3079 CNRS, Site Haute Température, 1D avenue de la Recherche Scientifique, 45071 Orléans, France

□ Corresponding author. E-mail address: raphael.schneider@univ-lorraine.fr

Abstract. The design and the synthesis of highly active nanohybrid photocatalysts for environmental remediation is a topical issue in the context of sustainable development. The hybridization of a semiconductor with noble metal nanoparticles (NPs) has been demonstrated to be a versatile strategy to restrict the recombination of photogenerated electron-hole pairs and thus increase the photocatalytic activity. However, the uniform association of nanosized metal particles with ZnO NPs remains a challenge. Herein, a novel synthesis of ZnO NPs hybridized with Ag(0) NPs is presented. Ag^+-doped layered zinc hydroxides (LZHs) were prepared in aqueous solution in the presence of triethanolamine and subsequently Ag^+ ions were photoreduced into metallic Ag NPs embedded into LZHs. The LZHs not only promote the dispersion of Ag NPs but also limit their growth. The Ag(0)-doped LZHs obtained after hydrothermal treatment was finally transformed into ZnO/Ag

nanohybrids by a mild thermal treatment at 300°C for 5 min, which allows high interface coupling between ZnO and Ag NPs. ZnO associated with 3 mol% Ag exhibits the highest photocatalytic activity for the degradation of dyes (Rhodamine B and Remazol Brillant Blue R) and of the Ciprofloxacin antibiotic. The high photocatalytic performance of the ZnO/Ag(3) nanohybrid originates from the charge transfer in the ZnO/Ag nanohybrid and from the enhanced harvesting of visible light. The ZnO/Ag(3) photocatalyst also exhibits a high practical stability, indicating its great potential for real photocatalytic applications.

Keywords : ZnO, Ag, nanohybrid, charge transfer, photocatalyst, degradation

1. Introduction

In recent years, semiconductor photocatalysis has gained high interest because this technology affords almost ideal solutions for environmental decontamination and energy shortages [1-5]. However, the photocatalytic activity of most metal oxide semiconductors like TiO_2, ZnO, ZrO_2, CeO_2 or Bi_2O_3 is limited by the fast recombination of charge carriers and their photoactivation, usually limited to the UV range that accounts only for ca. 4% of the solar spectrum. Therefore, it is important to develop novel sunlight photoactivable photocatalysts with high charge carrier separation properties.

ZnO is one of the most commonly used photocatalysts due to its high photosensitivity, high electron mobility (155 $cm^2\ V^{-1}\ s^{-1}$), low cost and weak toxicity [6-9]. However, its direct bandgap of 3.3 eV restricts its photoactivation to the UV region. Moreover, the fast recombination of photogenerated electron-hole pairs hinders its photocatalytic activity. Recently, increasedattention has been paid to the improvement of ZnO photocatalytic performance by delaying the recombination rate of photogenerated electron-hole pairs and enhancing the visible light absorption. This can be achieved by building a heterojunction between ZnO and other semiconductors [10-14], with graphene-based materials [15-18] or by hybridizing ZnO with noble metal NPs such as Ag, Au, Pd or Pt [19-24]. The association between Ag and ZnO not only improves the visible light absorption via local surface plasmonic resonance (LSPR) but also hinders the electron-hole recombination because Ag acts as an electron sink [19,20,25,26]. Moreover, the creation of a Schottky barrier at the ZnO-Ag interface allows the improvement of the electron-hole separation and thus of the

photocatalytic activity [19,20,25,26]. Numerous methods have been developed to prepare ZnO/Ag nanohybrids like precipitation [27-29] or sol-gel [30-32] followed by calcination, precipitation followed by Ag^+ reduction using sodium borohydride [33], photodeposition of Ag NPs on preformed ZnO [20,34], or biosynthesis [35]. Most of these methods usually allow a modest control of both the size of the produced ZnO and Ag NPs and of the Ag NPs dispersion at the surface of ZnO.

Layered zinc hydroxides (LZHs), prepared using $Zn(NO_3)_2$ as a precursor, are represented by the general formula $(Zn^{2+})_x(OH^-)_{2x-y}(NO_3^-)_y.nH_2O$, where NO_3^- is the intercalated anion [36,37]. Their structure includes a layer with octahedrally coordinated Zn^{2+} cations, in which a quarter of the octahedral positions are vacant allowing the formation of tetrahedrically coordinated cationic centers located above and below the octahedral sheet. Intercalated NO_3^- anions coordinate to tetrahedral Zn^{2+} cations and thus orient the structure to form a sequence of alternating zinc hydroxide and intercalated anionic layers [38-40]. LZHs have attracted high interest for their interlayer chemistry and have found applications in various fields such as adsorption, drug delivery and catalysis [36,37,41,42]. LZHs are also valuable precursors of nanostructured ZnO via thermal decomposition, usually conducted under air at temperatures varying between 450 and 900°C [38,40,43-45].

Herein, we report the first preparation of Ag^+-doped LZHs via a hydrothermal method combined with the photoreduction of Ag^+ ions into Ag NPs. The LZHs not only limit the growth of Ag(0) NPs but also promote their dispersion within LZHs and thus increase the interface coupling. The LZHs/Ag nanohybrids were converted into ZnO/Ag nanohybrids using a mild calcination at 300°C for 5 min. This synthetis strategy leads to very small Ag NPs (ca. 2.7 nm) hybridized with ca. 87 nm-sized ZnO NPs. Such nanohybrids can only be prepared using polymers networks as templates [20], a method which requires a post-synthetic high temperature calcination to remove the template, or using a photocatalytic support like graphene oxide which is able to chelate Ag^+ ions and restrict the growth of Ag(0) NPs [46]. The O-defective produced ZnO associated with 3 mol% Ag(0) NPs was demonstrated to be a highly active photocatalyst under simulated solar light irradiation for the degradation of dyes (Rhodamine B or Remazol Brilliant Blue R) and of the Ciprofloxacin antibiotic. The high photocatalytic activity was demonstrated to originate from Ag NPs acting as electron sink and allowing an efficient charge separation and from the enhanced visible light absorption

originating from LSPR. The ZnO/Ag(3) photocatalyst was also demonstrated to be of high stability and could be reused up to twelve times without significant alteration of its activity.

2. Experimental section

2.1. Materials and instruments

$Zn(NO_3)_2 \bullet 6H_2O$ (Merck, >99%), $AgNO_3$ (Alfa Aesar, 99.9%), triethanolamine (TEA, Acros Organics, 99%), tert-butanol (t-BuOH, Merck, >99%), 1,4-benzoquinone (BQ, Fluka, >98%), ammonium oxalate (AO, Merck, >99%), DMSO (Merck, >99.9%), catalase (Merck), sodium azide (Merck, >99%), Rhodamine B (RhB, Merck, analytical standard), Remazol Brilliant Blue R (RBBR, Merck), Ciprofloxacin (CIP, Merck, >98%) and absolute ethanol (VWR) were used as obtained.

X-ray diffraction (XRD) measurements were conducted using a Panalytical X'Pert pro MPD diffractometer with Cu Kα radiation. Morphological properties were investigated using scanning electron microscopy (SEM) (JEOL JSM-6490 LV and JEOL JSM IT800 instruments), and transmission electron microscopy (TEM) (Philips CM200 equipment operating at an acceleration voltage of 200 kV). Energy dispersive X-ray spectra (EDX) and elemental mappings

were obtained using the SEM instruments.

A Malvern Zetasizer Nano ZS equipment was used to determine the Zeta potential of the catalysts.

UV-visible absorption spectra were recorded on a Thermo Scientific Evolution 220 spectrometer. UV-visible diffuse reflectance spectra (DRS) of powders were measured using a Shimadzu 2600-2700 spectrometer. Fourier transform infrared (FT-IR) spectra were acquired on an ALPHA Brucker Optik spectrometer in the 4000-450 cm^{-1} wavenumber range. Raman spectra were recorded using a Xplora spectrometer from Horiba Scientific using a 532 nm Nd:YAG laser.

For LC-UV-MS analysis, high performance liquid chromatography system (Dionex Ultimate 3000, Thermo Fisher Scientific, France) was coupled to a dual-pressure linear ion trap mass spectrometer (LTQ Velos Pro, Thermo Fisher Scientific, MA, USA). C18 reverse phase column was used (Accucore^{TM} XL C18, 2.1 x 100 mm, 4 µm, Thermo Fisher Scientific, France) at a

constant temperature of 30°C. 20 µL of sample were injected. The flow rate was kept at 250 µL.min^{-1} during the LC run. For 8 min, the mobile phase was held at 5% acetonitrile / 95% water (+ 0,1% HCOOH) before applying a linear elution gradient to reach 100% acetonitrile at 17 min. All along a LC run, the flow was split 2 ways at the same flow rate (125 µL.min^{-1}), one for UV detection at a 275 nm wavelength and the other for mass spectrometry detection. HESI (Heated Electrospray Ionization Source) was selected as the ion source of the mass spectrometer. A voltage of 5 kV with N_2 as a nebulizer gas was applied to the capillary at a temperature of 210°C. MS system ran from 90 to 1000 m/z at a MS scan rate of 33333 m/z.s^{-1} in positive detection mode. To confirm chromatographic peak assignment, MS^2 and MS^3 by CID at 25 eV was systematically conducted on the most intense mass peak of each mass spectrum.

The initial and final total organic carbon (TOC) content was determined using a Shimadzu TOC-V_{CSH} analyzer to evaluate the photomineralization degree.

The photoelectrochemical tests were controlled with a potentiostat (BioLogic SP150) using a conventional three-electrode cell consisting in a Ag/AgCl electrode in saturated KCl as reference electrode and a Pt coil counter electrode. The working electrodes (FTO glass coated with ZnO or ZnO/Ag NPs) were exposed to simulated solar light irradiation (1 sun) provided by a 500W Xe lamp fitted with an AM 1.5G filter. The effective area of the electrodes was 1 cm^2 for all experiments. Photocurrent transient responses were evaluated from chronoamperometric measurements (i(t)) at a constant potential of + 0.5 V vs Ag/AgCl in a 0.1 M Na_2SO_4 electrolyte solution. Potentiostatic electrochemical impedance spectroscopy (EIS) was conducted from 500 kHz to 10 mHz for low amplitudes of ± 10 mV at open circuit potential (OCP).

2.2. Synthesis of ZnO/Ag nanohybrid photocatalysts

The representative procedure for the preparation of the ZnO/Ag(3) catalyst is as follows. Firstly, $Zn(NO_3)_2$ (29.1 mmol) and $AgNO_3$ (0.9 mmol) were solubilized in 36 mL of water under magnetic stirring and the mixture was further stirred for 10 min. Next, TEA (6 mL) was added dropwise and the mixture was further stirred for 10 min. The solution was then irradiated with a UV lamp (irradiance of 3 mW/cm^2 at 365 nm) for 2 h before being transferred to a Teflon lined autoclave and heated at 110°C for 2 h. After natural cooling to

room temperature, the obtained powder was washed with water (4 x 20 mL) and dried at 70°C overnight. Finally, the LZHs were converted into ZnO NPs by heating the powder at 300°C for 5 mins. The obtained solid was used without any further purification for characterization and photocatalytic experiments.

2.3. Photocatalytic activity

The photocatalytic performance of ZnO/Ag nanohybrids was evaluated for the degradation of Rhodamine B (RhB), Remazol Brilliant Blue R (RBBR) and Ciprofloxacin (CIP) used at a concentration of 10 mg/L. Photocatalytic degradations were conducted under simulated solar light irradiation (irradiance of 30 mW/cm^2 at 365 nm) and at room temperature. Firstly, 50 mL of the pollutant solution and 50 mg of the ZnO/Ag photocatalyst were stirred in the dark for 60 min to reach the adsorption-desorption equilibrium. Next, light was turned on and ca. 2 mL of the mixture were sampled after fixed time intervals, centrifuged (4000 rpm for 5 mins) and finally analyzed by UV-visible spectroscopy.
The active species involved in the photocatalytic degradation were determined using DMSO, t-BuOH, NaN_3, p-benzoquinone (BQ), ammonium oxalate (AO) and the catalase enzyme to capture electrons, hydroxyl $^{\bullet}OH$ radicals, singlet oxygen $^1O_2$, superoxide $O_2^{\bullet-}$ radicals, holes and hydrogen peroxide H_2O_2, respectively. All scavengers were used at a concentration of 10 mM, except BQ used at a concentration of 0.1 mM.

3. Results and discussion

3.1. ZnO/Ag catalysts synthesis from Ag^+-doped LZHs and structural characterization

The synthesis of Ag^+-doped LZHs was initiated at room temperature by adding TEA, used as bifunctional alkali source and as morphological controlling agent [47,48], to an aqueous mixture of $Zn(NO_3)_2$ and $AgNO_3$. Next, Ag^+ ions were photoreduced into Ag NPs and the growth of the LZHs was continued under hydrothermal conditions (2 h at 110°C) to embed Ag NPs into the LZHs (Scheme 1). UV-visible absorption spectra, recorded during the photoreduction of Ag^+ ions, clearly show the surface plasmon resonance of Ag(0) NPs (Fig. S1). Interestlingly, when this experiment was conducted in the absence of $Zn(NO_3)_2$, a

metallic Ag film appears about 30 min after the start of the irradiation, which shows that LZHs allow Ag NPs stabilization, while prevent their coalescence.

We also evaluated various calcination temperatures (250, 300, 350, 450 and 550°C) and various times (3, 5, 10 and 15 min) for the conversion of LZHs into ZnO. These preliminary experiments, not described herein, showed that ZnO/Ag nanohybrids exhibiting the highest photocatalytic activity were obtained after 5 min thermolysis at 300°C and these experimental conditions have been used throughout this work.

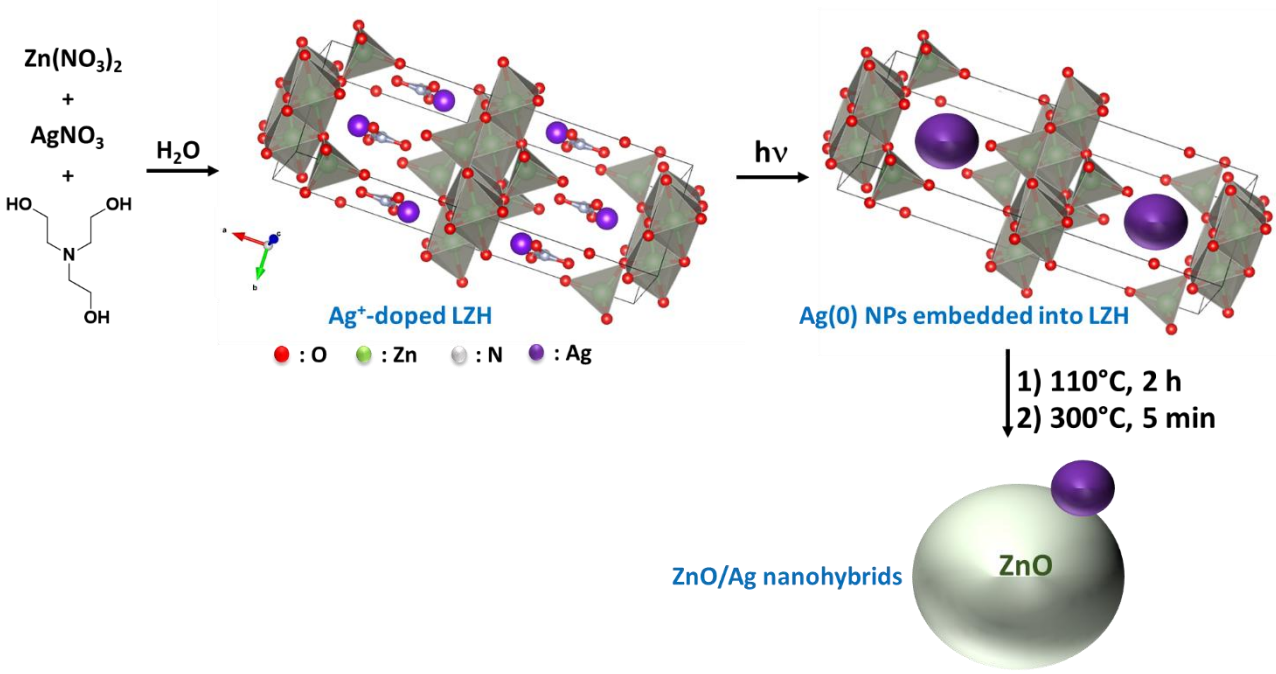

Scheme 1. Schematic representation of the synthetic strategy used to prepare ZnO/Ag nanohybrids from Ag^+-doped LZHs (the crystal structure proposed for the Ag^+-doped LZH has not yet been validated by XRD analysis).

SEM images of the pure LZH and of the 3% Ag^+-doped LZH show irregular sheets with an average size of ca. 5 µm and a thickness of ca. 300 nm (Fig. S2). These sheets are assembled into larger flowerlike structures up to 20 µm. The morphology of LZHs is not affected by the Ag^+-doping. The purity and the functional characteristics of Ag^+-doped LZHs, ZnO and ZnO/Ag catalysts were assessed by FT-IR. The FT-IR spectra of LZHs and Ag-doped LZHs are typical of these materials and show signals at 3582 cm^{-1} (OH groups in the LZH lattice), 3462 cm^{-1} (physisorbed H_2O molecules), 1642 cm^{-1} (bending OH groups), 1369 cm^{-1} (NO_3^- groups) and peaks at 469 and 434 cm^{-1} (stretching of Zn-O bonds) (Fig. S3) [49]. All these signals

disappear after heating the LZHs at 300°C for 5 min and only a strong signal at ca. 475 cm^{-1} corresponding to the Zn-O stretching in ZnO NPs could be observed (Fig. S4) [50]. The other weak signals observed on the FT-IR correspond to remainings of TEA not fully removed from the surface of the ZnO NPs after the 5 mins heating at 300°C.

XRD shows that the organization of tetrahedral units in LZHs and Ag^+-doped LZHs is similar to that of monoclinic $Zn_5(NO_3)_2(OH)_8.2H_2O$ (JCPDS No 00-024-1460) (Fig. S5 and S6) [51]. After conversion by thermolysis into ZnO, the XRD patterns of the ZnO/Ag NPs correspond to the crystal planes of hexagonal wurtzite ZnO structure (JCPDS No 79-0207) and no additional peaks corresponding to metallic Ag or AgO could be detected, likely due to the weak Ag-loading of the nanohybrids, their small size and high dispersion at the surface of ZnO NPs (*vide infra*) (Fig. 1a). The broadness of the peaks suggests the formation of small sized ZnO crystals. With the increase of the Ag loading percentage from 1 to 10 mol%, the position of the (101) peak is shifted toward lower 2θ values, indicating that a small part of Ag^+ ions have not been reduced into Ag(0) NPs but loaded into the ZnO NPs. The observed shift originates from the partial substitution of Ag^+ ions in the ZnO crystal lattice accompanied by the increase of the a and c lattice parameters due to the higher ionic radius of Ag^+ (0.126 nm) compared to Zn^{2+} (0.074 nm) (Fig. 1b). As previously shown, Ag^+ ions behave as monovalent dopants like Li^+ or Na^+ and may substitute Zn^{2+} ions in the ZnO lattice or occupy interstitial sites [52].

Raman spectra were recorded using a 532 nm laser light source to gain further information about the crystallinity of ZnO/Ag nanohybrids (Fig. 1c). The hexagonal wurtzite structure of ZnO belongs to the $P6_3mc$ space group which generates Raman-active phonon modes at 325 (*2E2* M), 382 (*A1* TO), 387 (*E1* TO), 436 (*E2* high), 574 (*A1* LO) and 583 cm^{-1} (*E1* LO) of first order [53]. These signals can be observed for ZnO/Ag nanohybrids, indicating that the crystalline structure of ZnO was not markedly affected, which agrees well with XRD results. However, with the increase of the Ag(0) NPs loading on ZnO and of the doping of Ag^+ ions in the ZnO crystal lattive, the Raman signals become broader and their intensity decreases, indicating an alteration of the crystallinity, likely originating from the increase of defect density (Zn vacancies V_{Zn}, O vacancies V_O and interstitial Zn Zn_i). The signal at ca. 563 cm^{-1} linked to surface V_O defects notably increases, which should favor photocatalytic activity (*vide infra*) [30].

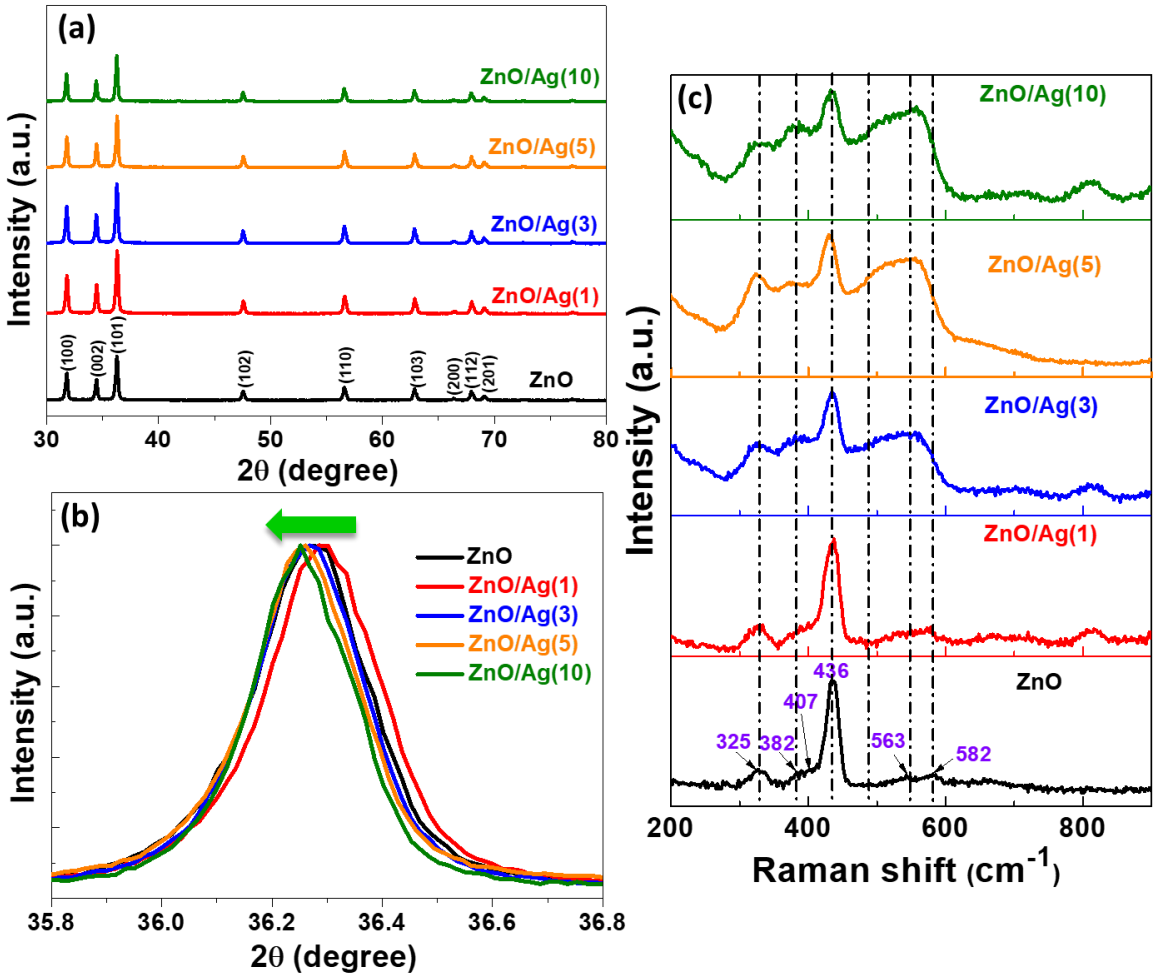

Fig. 1. (a) XRD patterns of ZnO and ZnO/Ag heterostructures, (b) magnification showing the shift of the (101) peak when increasing the Ag loading, (c) Raman spectra of ZnO and ZnO/Ag heterostructures.

The composition and chemical states of the elements present in ZnO/Ag(3) NPs were further investigated by XPS. As can be seen from the survey XPS spectrum (Fig. 2a), only Zn, O, Ag and C elements could be detected. Considering that C originates from the hydrocarbon impurities present in the instrument, the ZnO/Ag(3) catalyst shows a high purity. The Zn $2p_{3/2}$ and Zn $2p_{1/2}$ signals are located at 1023.52 and 1046.73 eV, respectively, indicating that Zn is present at the +2 oxidation state (Fig. 2b). There is a noteworthy shift of Zn 2p peaks toward high energy compared to pure ZnO (1044.3 and 1021.1 eV for Zn $2p_{5/2}$ and Zn $2p_{3/2}$, respectively) [54], which can be attributed to the electron transfer between ZnO and Ag NPs [55]. The O 1s spectrum can be deconvoluted into two signals located at 530.52 and 532.19 eV corresponding to O atoms in the ZnO crystal lattice and to V_O, respectively (Fig. 2c) [56].

As water molecules can dissociatively adsorb on V_O to form surface hydroxyl groups, the presence of these V_O should improve the photocatalytic activity. The Ag $3d_{5/2}$ and Ag $3d_{3/2}$ peaks are located at 367.9 and 373.9 eV, respectively, and the Ag 3d energy splitting is of 6 eV, which confirms the presence of metallic silver (Fig. 2d) [57]. Ag in the +1 oxidation state was not detected by XPS probably because Ag^+ ions doped in ZnO are not located near the surface but in the core of ZnO NPs.

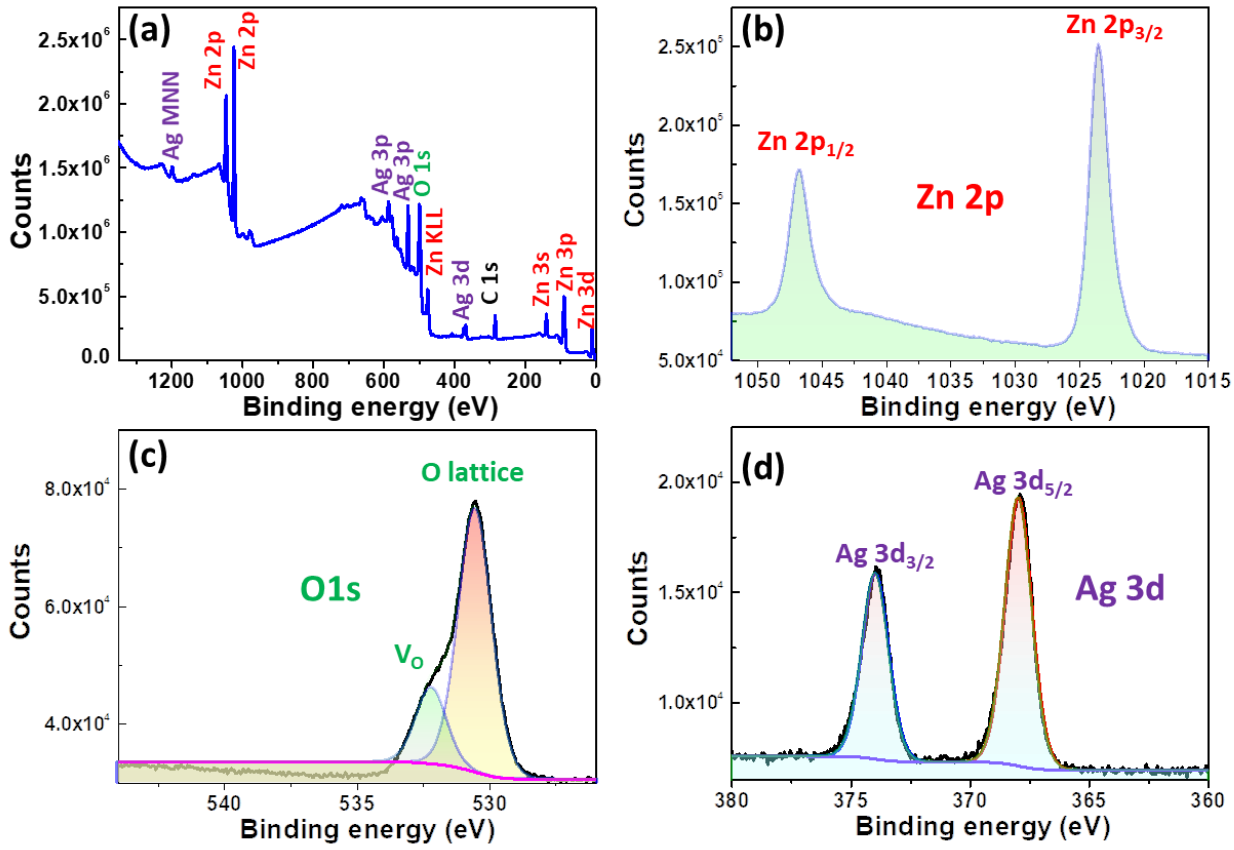

Fig. 2. (a) XPS survey spectrum. High resolution XPS spectra of (b) Zn 2p, (c) O 1s and (d) Ag 3d.

SEM images show that ZnO and ZnO/Ag photocatalysts are composed of tray-shaped particles up to 400 nm-long and a thickness of a few tens of nanometers (Fig. S7). No significant difference in morphology is observed when varying the Ag(0) NP loading. The elemental composition of ZnO and ZnO/Ag catalysts was determined by EDX analysis (insets of Fig. S7). The signals at ca. 0.5 and 1 keV can be assigned to O and Zn elements, respectively. Only weak signals between 2.6 and 3.2 keV could be observed for Ag due to the

low Ag loading in the ZnO/Ag nanohybrids. These results further confirm the successful preparation of ZnO/Ag catalysts.

TEM images of the ZnO/Ag(3) sample selected as a representative shows the presence of ellipsoidal ZnO NPs with an average diameter of ca 87.0 ± 14 nm (Fig. 3a), indicating that the particles observed by SEM are made up of associated ZnO/Ag nanohybrids. The selected area electron diffraction (SAED) pattern shows rings corresponding to the planes of hexagonal ZnO (inset of Fig. 3a), which agrees with XRD results. The HR-TEM image indicates that Ag NPs with an average size of 2.7 ± 0.3 nm are well dispersed at the surface of ZnO (Fig. 3b). The spacings between the lattice fringes determined from the HR-TEM image are of 0.30 nm and 0.24 nm (Fig. 3c), which is in accordance with the interplanar spacing between the (100) lattice planes of the ZnO wurtzite phase and (111) lattice planes of face-centered cubic Ag(0), respectively. TEM results show that the thermal decomposition of the Ag-doped LZH, accompanied by the evaporation of TEA, causes total dislocation of LZH sheets into ZnO and Ag NPs. The SEM-EDX mapping shows the presence of Zn, O and Ag elements (Fig. 3d-g) and further demonstrates that Ag NPs are well associated with ZnO.

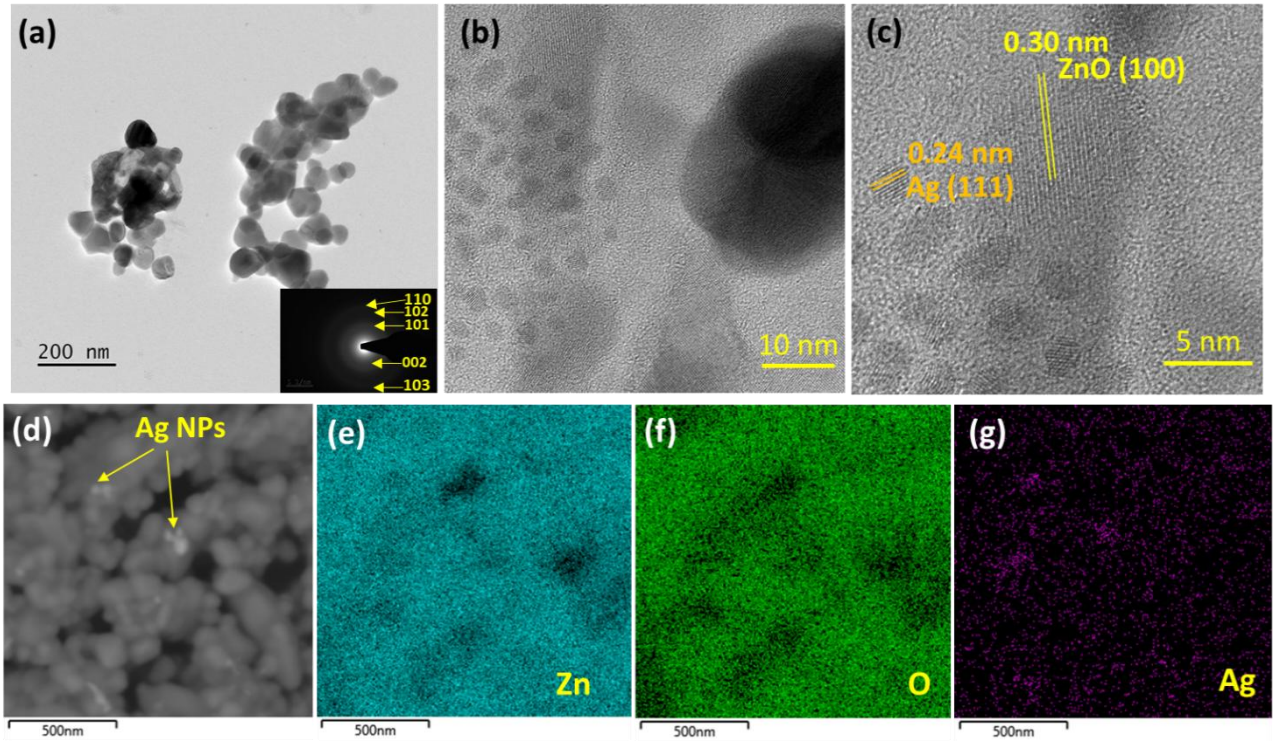

Fig. 3. (a,b) TEM and (c) HR-TEM images of the ZnO/Ag(3) photocatalyst. (d) SEM image of the ZnO/Ag(3) catalyst, and EDX elemental mapping of (e) Zn, (f) O and (g) Ag elements.

BET measurements were conducted to determine the specific surface area of ZnO and ZnO/Ag nanohybrids (Fig. S8). The nitrogen adsorption-desorption isotherms are of type IV according to the IUPAC classification, indicating the presence of mesopores. The determined BET surface areas are modest (8.23, 7.19, 8.08, 7.68 and 8.45 m^2/g for ZnO, ZnO/Ag 1, 3, 5 and 10 samples, respectively), which further confirms that the porous structure of LZHs was not transfered to ZnO after calcination.

3.2. Optical and photo-electronic properties

As can be seen from Fig. 4a, pure ZnO has an optical absorption edge at ca. 400 nm, indicating that it should only be active as a photocatalyst under UV light irradiation. Pure Ag(0) NPs prepared by photoreduction in the absence of $Zn(NO_3)_2$ show a broad absorption band from 300 to 750 nm with a maximum at ca. 450 nm, originating from the LSPR [58]. With the increase of the Ag loading in ZnO/Ag nanohybrids, the visible light absorption gradually increases due to the LSPR of Ag NPs at ca. 470 nm, which can only clearly be observed for the samples doped with 5 and 10 mol% Ag. The energy bandgaps were determined from the UV-visible absorption spectra by Tauc's plot using the equation $\alpha h\gamma = A(\alpha h\gamma - Eg)^2$ where *Eg* is the bandgap energy, *h* is the Plank's constant and α is the absorption coefficient. *Eg* values are of 3.23, 3.21, 3.19, 3.18 and 3.17 eV for ZnO and ZnO/Ag 1, 3, 5 and 10 samples, respectively. These results indicate that ZnO/Ag nanohybrids absorb more visible light energy and should thus produce more photogenerated charge carriers under solar light illumination, which should favor the photocatalytic activity. The decrease of the bandgap observed for ZnO/Ag samples may be related either to the interfacial electron coupling between ZnO and Ag NPs [59] or to the increase of V_O in the ZnO crystal structure as previously proposed by Sarma *et al*. [60], which agrees with the Raman spectra. These defects can reduce the recombination of charge carriers in ZnO/Ag hybrids and thus enhance the separation of photo-generated electrons and holes at the interface of heterostructured ZnO/Ag photocatalysts.

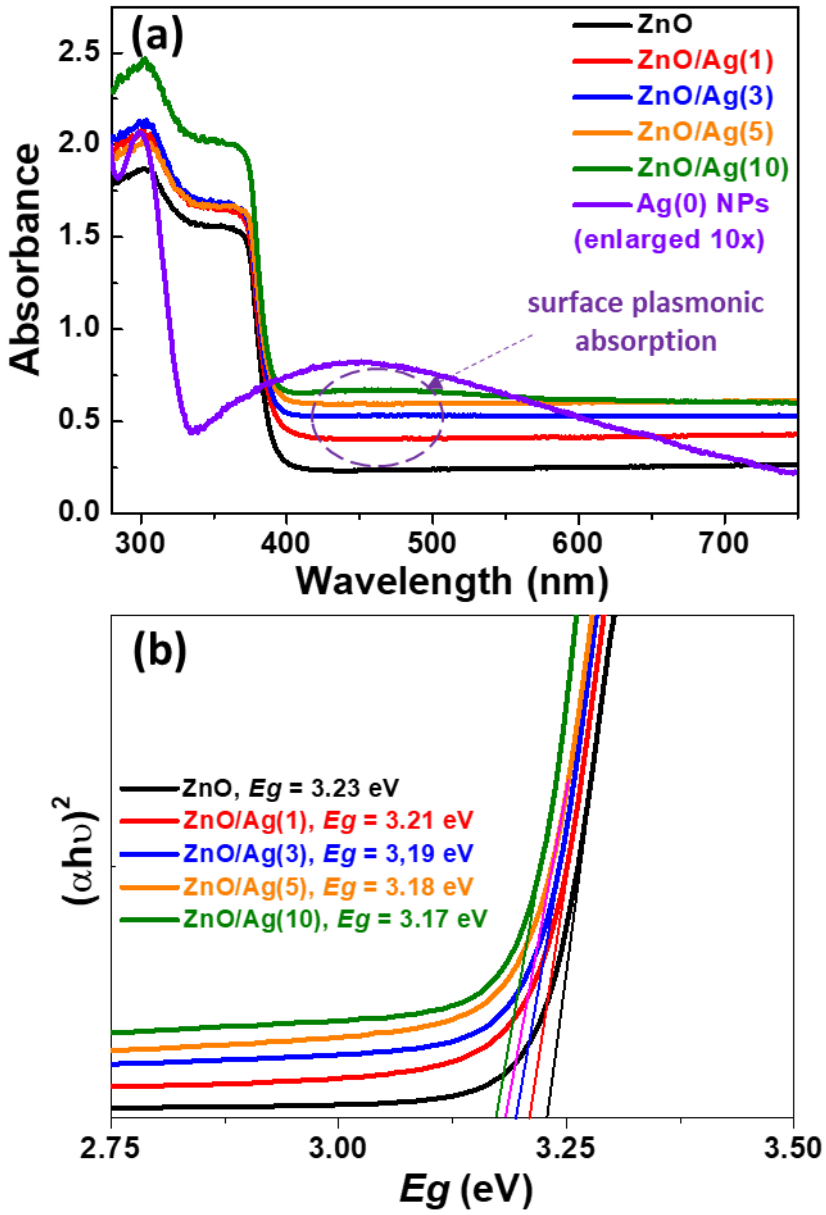

Fig. 4. (a) UV visible absorption spectra of Ag(0) NPs and of ZnO and ZnO/Ag catalysts and (b) Tauc's plots used to determine *Eg* values of ZnO and ZnO/Ag catalysts.

Fig. 5a shows the PL emission spectra at room temperature of ZnO and ZnO/Ag catalysts after excitation at 370 nm. For pure ZnO, a single and broad emission centered at ca. 590 nm can be observed. This orange-red emission originates from singly ionized O vacancies and/or transition of holes from the valence band to the preexisting deep donor energy level [61,62]. The PL emission maximum and the shape of the PL signal of ZnO/Ag hybrids are similar to those of ZnO but their intensities decrease gradually with the increase of the Ag loading,

indicating that the charge recombination is hindered. This originates from the presence of Ag NPs that act as sink of photogenerated electrons in ZnO. The conduction band of ZnO is higher in energy than the Fermi energy level of Ag NPs (*vide infra*) and thus photogenerated electrons in ZnO can easily transfer to Ag NPs, which hinders the recombination in excitons.

The photogenerated electron-hole transfer performance was further characterized using transient photocurrent response. Fig. 5b displays the photocurrent density of ZnO and ZnO/Ag NPs deposited on FTO substrates under on/off cycles of simulated solar light irradiation. As can be seen in Fig. 5b, a sharp increase of the photocurrent is detected when the light is turned on and that phenomenon is reversible when light is switched off. The photocurrent increases with Ag loading from 1 to 3 mol% and then decreases for ZnO/Ag(5) and ZnO/Ag(10) heterostructures. The photocurrent of the ZnO/Ag(3) photoelectrode is ca. 2.8 times higher than that of ZnO. These results show improved separation of photogenerated electrons and holes for ZnO/Ag nanohybrids, which originates from a synergetic effect between ZnO and Ag NPs.

Electrochemical impedance spectroscopy (EIS) was further used to explore the charge-transport resistance. As seen in Fig. 5c, the ZnO/Ag(3) catalyst has the smallest arc radius, indicating a fast charge carrier transfer that promotes the photogenerated charge separation and should thus improve the photocatalytic activity. Nyquist plots were fitted using a simplified Randles circuit to determine the charge transfer resistance R_{CT} (see Table S1). As expected, the R_{CT} value is weakest for the ZnO/Ag(3) NPs, which further confirms that the charge transferability is highest for this particular catalyst.

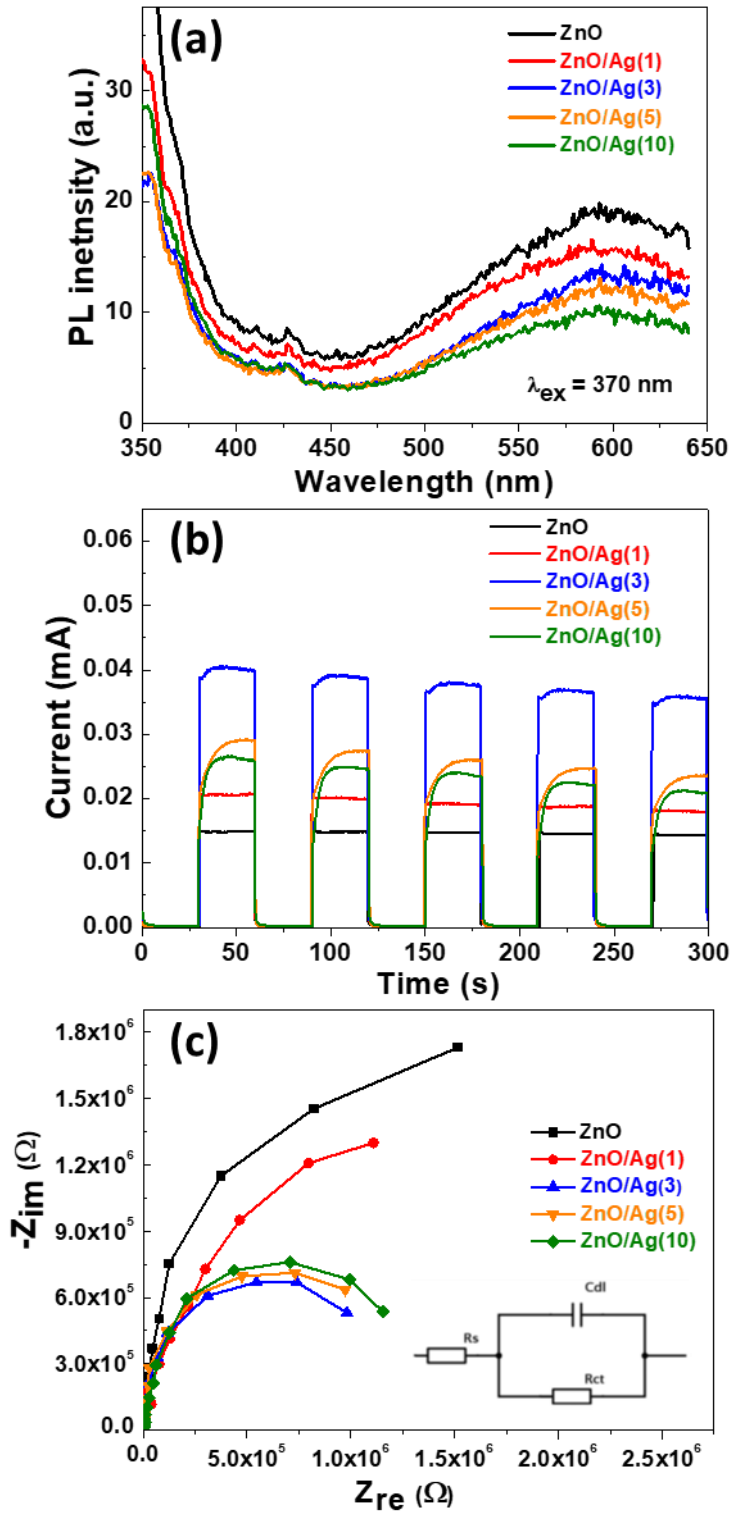

Fig. 5. (a) PL emission spectra, (b) transient photocurrent responses and (c) EIS Nyquist plots of ZnO and ZnO/Ag photocatalysts. Inset : Randles equivalent circuit model.

3.3. Photocatalytic activity

The surface charge of the photocatalyst plays an important role on the photocatalytic degradation of pollutants because it conditions their adsorption on the surface of the catalyst. Fig. S9 shows the surface Zeta potential vs pH of ZnO and ZnO/Ag(3) catalysts. The pH of the point of zero charge (pzc) of ZnO is 8.8, a value consistent with previous reports [63]. A slight decrease of the pzc is observed upon association with Ag NPs, likely due to the presence of residues of positively charged TEA at the surface of Ag NPs.

We first investigated the ability of ZnO/Ag photocatalysts to decompose RhB under simulated solar light illumination (light irradiance of 30 mW/cm^2) (Fig. 6a). At pH 7, less than 3% of RhB is adsorbed at the surface of the catalyst during the 60 mins stirring in the dark due to the electrostatic repulsion between the both positively-charged dye and photocatalyst. After turning on the light, a fast photocatalytic degradation of RhB is observed for ZnO associated to 3, 5 and 10% Ag, the decomposition being almost complete after 45 min for ZnO/Ag(3) and ZnO/Ag(10) catalysts. The photocatalytic degradation kinetics of RhB using ZnO and ZnO/Ag catalysts can be fitted with a first-order Langmuir-Hinshelwood model described by the equation $\ln(C_0/C) = kt$ where C_0 and C are the initial and at time t concentrations of RhB, respectively, and k is the first-order rate constant of the photocatalytic degradation. The k values determined for ZnO, ZnO/Ag(1), ZnO/Ag(3), ZnO/Ag(5) and ZnO/Ag(10) catalysts are 0.014, 0.036, 0.146, 0.092 and 0.100 min^{-1}, respectively, which further confirms that the ZnO/Ag(3) catalyst exhibits the highest activity (Fig. S10). Fig. 6b shows the UV-visible absorption spectra of RhB during its photocatalytic degradation using the ZnO/Ag(3) catalyst at different time intervals. The disappearance of all absorption peaks in the 250-600 nm range confirms the complete decomposition of the dye.

The influence of the pH on the photocatalytic degradation of RhB was also investigated as it influences both the adsorption of the dye at the surface of the catalyst and the reactive species present in solution [64]. Results presented in Fig. S11 show that the photocatalytic degradation efficiency of RhB is only weakly influenced when the pH of the solution was varied between 5 and 11. A decrease of the degradation rate is observed at pH 3 likely due to the acidic and/or photochemical corrosion of the ZnO/Ag(3) catalyst.

Next, the ability of the ZnO/Ag(3) catalyst to decompose RBBR was investigated (Fig. 6c and Fig. S12). During the 60 min of stirring in the dark, ca. 30% of the dye was adsorbed at the

surface of ZnO and ZnO/Ag(3) NPs due to electrostatic interaction between the negatively charged RBBR dye and the catalysts. The photocatlytic degradation of RBBR is complete in 30 minsusing the ZnO/Ag(3) catalyst, while only 60% of the dye is decomposed after the same irradiation time using ZnO NPs. The k values values determined using the slopes of $\ln(C_0/C)$ vs t (0.123 and 0.032 min^{-1} for ZnO/Ag(3) and ZnO, respectively) show that the activity of the ZnO/Ag(3) catalyst for the degradation of RBBR is ca. 3.8 times higher than that of ZnO (Fig. S13).

Finally, the photocatalytic degradation of the colorless CIP drug was investigated. CIP is a second-generation fluoroquinone antibiotic commonly used in veterinary and human medication to fight against microorganism proliferation. The bioaccumulation of CIP increases antibiotic resistance and threatens both aquatic ecosystems and human health [65]. As can be seen from Fig. 6d and Fig.S14, 98% of CIP is decomposed after 40 mins irradiation using the ZnO/Ag(3) catalyst while the same percentage of degradation is achieved only after 90 mins of irradiation using ZnO NPs. The k values determined for ZnO/Ag(3) and ZnO are 0.093 andd 0.039 min^{-1}, respectively (Fig. S15), further indicating that the activity of the ZnO/Ag(3) catalyst is markedly enhanced compared to ZnO.

The influence of the CIP concentration (5, 10 or 20 mg/L) on the photocatalytic performance of the ZnO/Ag(3) nanohybrid was also investigated (Fig. S16). As expected, a decrease of the degradation rate is observed when increasing the CIP concentration (30, 40 and 90 min for concentrations of 5, 10 and 20 mg/L, respectively) due to the saturation of the photocatalytically active sites by CIP and the intermediates produced during the photodegradation.

The performance of the ZnO/Ag(3) catalyst for the degradation of CIP was compared to recently developed ZnO-based photocatalysts and the results are described in Table S2. Although the CIP or catalyst concentrations and irradiation conditions are different from those used in this study, the ZnO/Ag(3) catalyst is very competitive with those reported in the literature for the degradation of CIP.

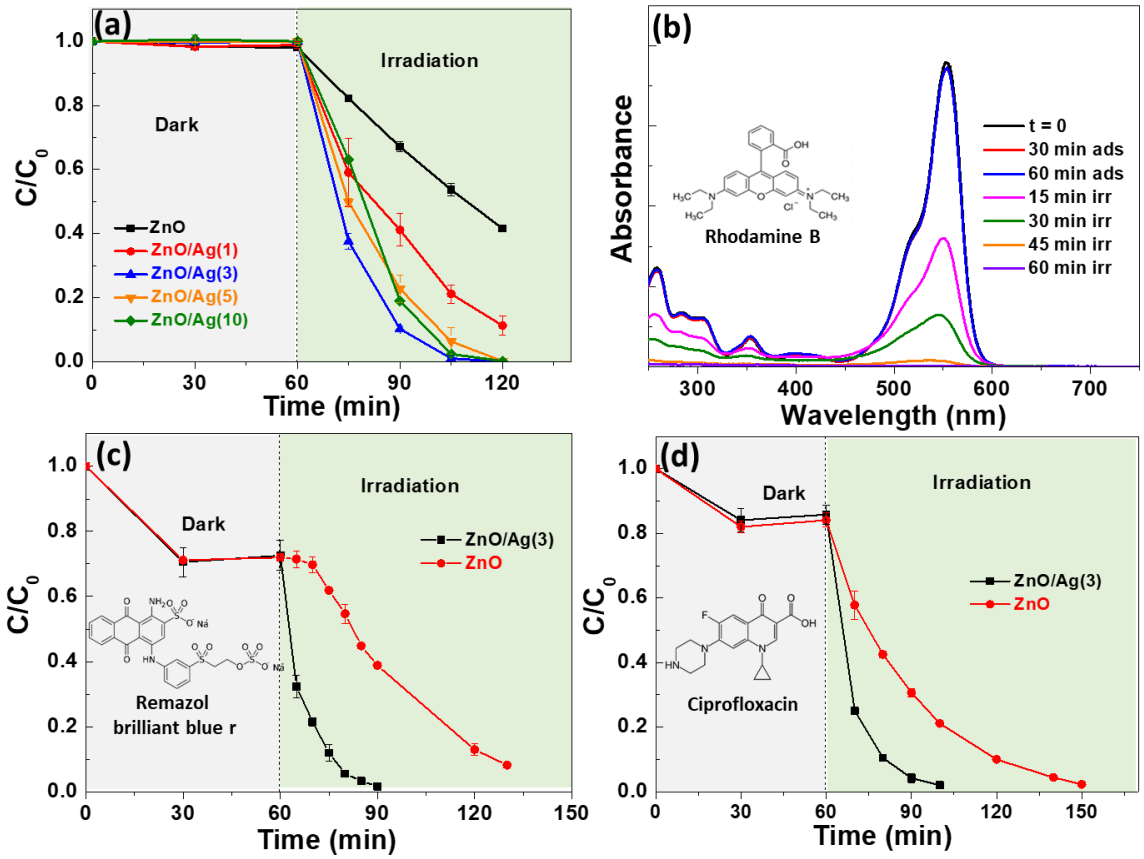

Fig. 6. (a) Evaluation of the photocatalytic properties of ZnO/Ag nanohybrids for the degradation of RhB under solar light irradiation, (b) UV-visible absorption spectra of RhB during its photodegradation using the ZnO/Ag(3) catalyst, Evaluation of the photocalytic performance of ZnO and ZnO/Ag(3) NPs for the degradation of (c) RBBR and (d) CIP.

3.4. CIP photodegradation mechanism

To determine the CIP photocatalytic degradation mechanism, the intermediates formed during the 40 first minutes of irradiation were determined by liquid chromatography coupled to UV detection and mass spectrometry (Scheme 2). Chromatograms obtained using UV detection are provided in Fig. S17. Using LC-MS results, three degradation pathways can be proposed for the degradation of CIP. All compounds are detected as protonated ($[M+H]^+$). The results obtained show that the carbon-fluorine bond (pathway 1), the piperazine moiety (pathway 2) and the carboxylic acid function (pathway 3) are the first functional groups affected by the reactive species generated during the photocatalysis.

In pathway 1, the C-F bond is firstly transformed into a C-O bond (m/z = 330), then a photo-cleavage of the piperazine ring results in an aminophenol (m/z = 263). In pathway 2, an oxidation and opening of the piperazine occur thus generating a diamide (m/z = 362). After deformylation (m/z = 334) and C-N bond break, a monoamide (m/z = 291) is produced. Further deformylation affords the amine with a m/z of 263. The decarboxylation of CIP (m/z = 288) is the first step of pathway 3. As the TOC of the CIP solution is decreased by ca. 53% during the 40 mins of irradiation in the presence of the ZnO/Ag(3) photocatalyst, the intermediates depicted in Scheme 2 are further decomposed in lower molecular weight compounds, H_2O, CO_2 and NO_3^-.

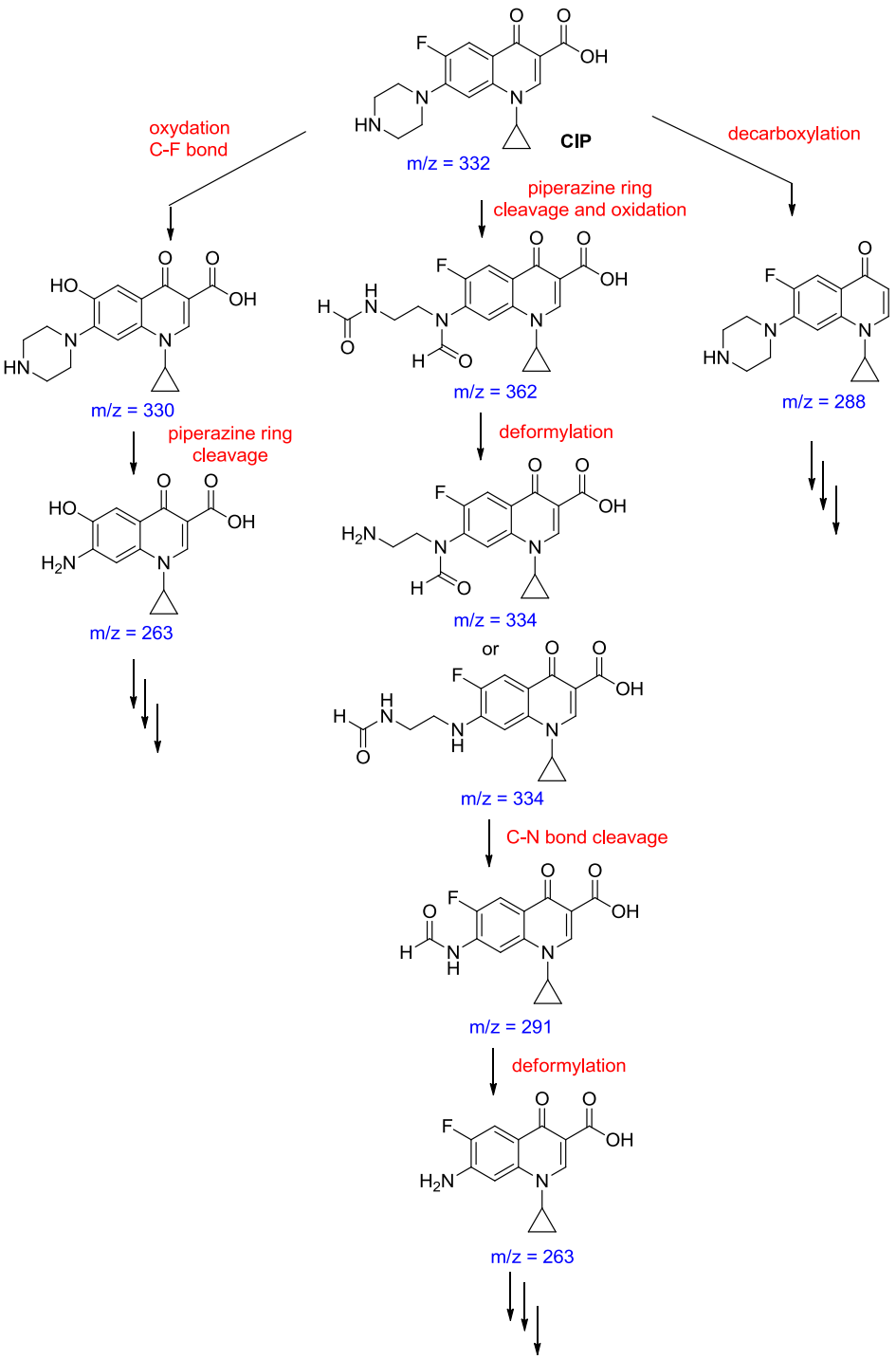

Scheme 2. Proposed degradation pathways of CIP using the ZnO/Ag(3) catalyst under simulated solar light irradiation.

3.5. Stability and reusability

The reusability and the stability of the ZnO/Ag(3) photocatalyst were also investigated for practical applications. For that purpose, the catalyst was used for the photodegradation of

RhB in twelve repeating cycles under simulated solar light irradiation. After each cycle, the photocatalyst was recovered by centrifugation and reused without any treatment. As shown in Fig. 7a, the photocatalytic degradation performance only weakly decreases after the twelve cycles (from 100 to 96%), indicating the high stability of the ZnO/Ag(3) catalyst for real environmental applications. XRD analyses confirm that the crystalline structure of the catalyst was not altered in these repeated uses (Fig. 7b). The FT-IR spectrum of the photocatalyst after the twelve cycles also shows that there are very few organic compounds adsorbed to its surface, confirming the effectiveness of the photocatalytic treatment (Fig. S18).

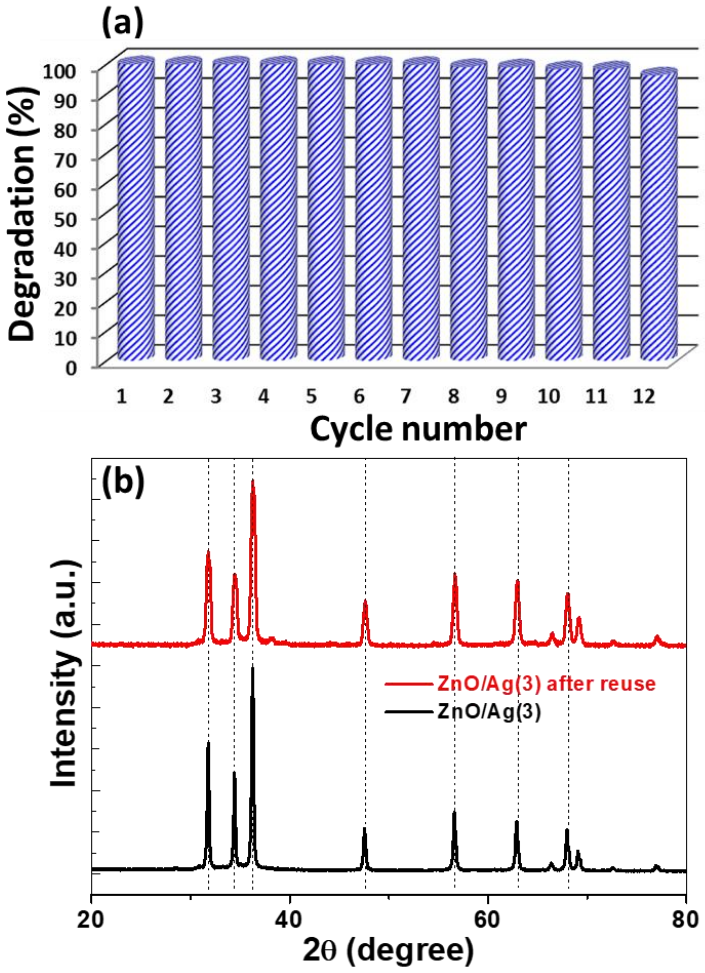

Fig. 7. (a) RhB degradation efficiency using the ZnO/Ag(3) photocatalyst cycles twelve times under simulated solar light irradiation, (b) XRD patterns of the as-prepared and of the reused ZnO/Ag(3) catalyst.

3.6. Photocatalytic mechanism

To determine the active species involved in the photocatalytic degradation of CIP using the ZnO/Ag(3) nanohybrid, scavenging experiments were carried out using DMSO, t-BuOH, NaN_3, p-benzoquinone (BQ), ammonium oxalate (AO) and the catalase enzyme to trap electrons, hydroxyl $^{\bullet}OH$ radicals, singlet oxygen $^1O_2$, superoxide $O_2^{\bullet-}$ radicals, holes and hydrogen peroxide H_2O_2, respectively. As shown in Fig. 8a, the photocatalytic degradation efficiency markedly decreases in the presence of BQ and catalase (7 and 37% degradation after a 60 min illumination), indicating that $O_2^{\bullet-}$ radicals and H_2O_2 are the species mainly involved in the decomposition of CIP. The deleterious effect of other scavengers is markedly lower, indicating the minor role played by electrons, $^{\bullet}OH$ radicals, $^1O_2$ and holes in the degradation.

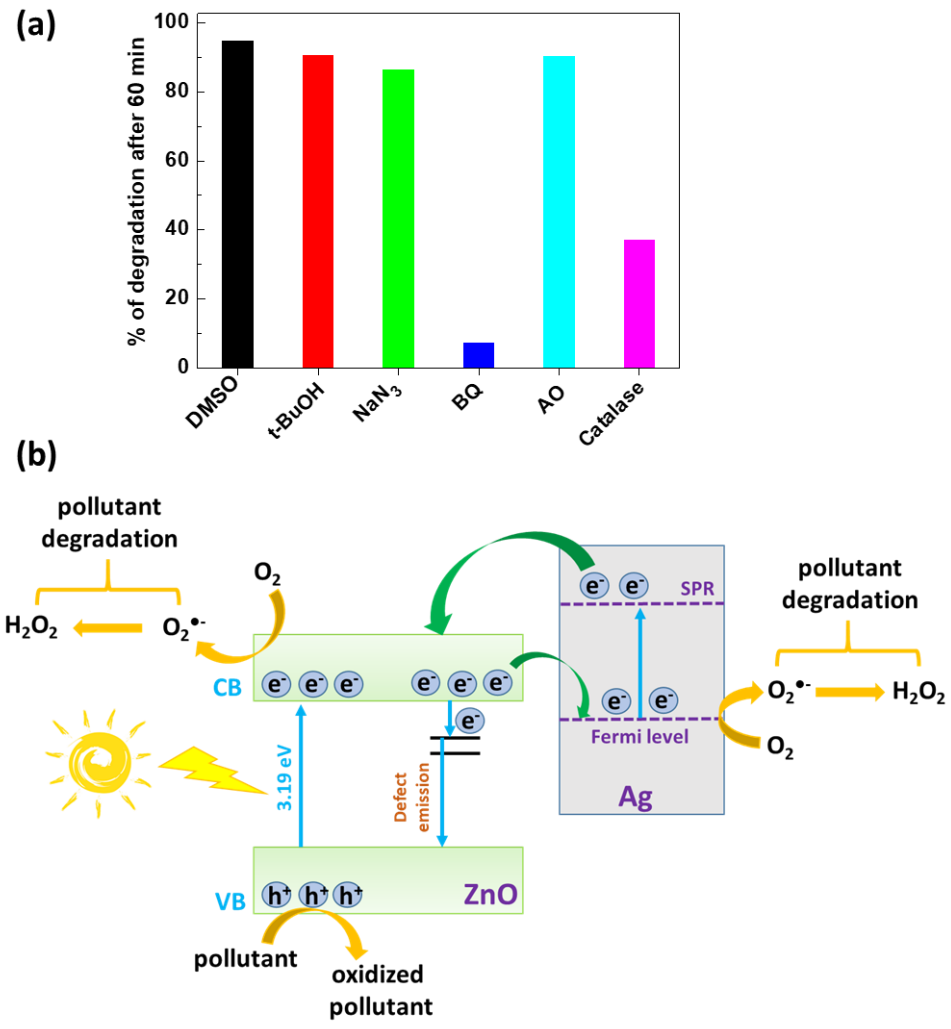

Fig. 8. (a) Performance of ZnO/Ag(3) NPs for the degradation of CIP in the presence of scavengers, (b) schematic representation of the photocatalytic mechanism using ZnO/Ag(3) NPs.

The valence band (E_{VB}) and the conduction band (E_{CB}) potentials of ZnO NPs were calculated using formula (1) and (2) :

$$E_{VB} = \chi - E^e + 0.5\ Eg \qquad (1)$$

$$E_{CB} = E_{VB} - Eg \qquad (2)$$

where χ is the absolute electronegativity of the semiconductor (5.89 for ZnO), Eg is the bandgap energy determined from UV-visible absorption spectra (3.19 eV for the ZnO/Ag(3) NPs), and E^e is the energy of free electrons on the hydrogen scale (ca. 4.5 eV) [66]. The values determined for E_{VB}(ZnO/Ag(3)) and E_{CB}(ZnO/Ag(3)) are 2.98 and -0.205 eV, respectively.

Due to the close contact of ZnO and Ag NPs, a Schottky barrier is established at the interface. Then, the Fermi levels of ZnO and Ag NPs combine to generate a new equilibrium state Fermi level [67,68]. Based on the previously described results, the following mechanism can be proposed for the solar light-mediated degradation of pollutants using the ZnO/Ag(3) photocatalyst (Fig. 8b). In a first step, the polluant adsorbs on the surface of the ZnO/Ag(3) catalyst. Upon light irradiation, photogenerated electron-hole pairs are produced in ZnO. Since the CB edge of ZnO (-0.205 eV vs NHE) is located close to that of the $O_2/O_2^{\bullet-}$ couple (-0.33 eV vs NHE), the photogenerated electrons are captured by O_2 molecules adsorbed at the surface of the catalyst to produce $O_2^{\bullet-}$ radicals that were demonstrated to be the main active specie involved in the degradation. The photogenerated electrons can also be transferred to Ag(0) NPs acting as electron sinks, which further allows the production of $O_2^{\bullet-}$ radicals after reacting with adsorbed O_2 molecules. These electrons may also react with O_2 to produce $HO_2^{\bullet}$ radicals as the standard redox potential of the $O_2/HO_2^{\bullet}$ couple is -0.05 eV vs NHE. $HO_2^{\bullet}$ radicals can further be reduced by electrons and protonated to yield H_2O_2 which is the second major specie involved in the photocatalytic degradation. $HO_2^{\bullet}$ radicals may also combine to form H_2O_2 and O_2 (Eq. 3).

$$HO_2^{\bullet} + HO_2^{\bullet} \rightarrow H_2O_2 + O_2 \qquad (3)$$

Upon light excitation, the electrons in Ag can also move from the Fermi level to the CB of ZnO via surface plasmons, allowing an increase of the electron density in the CB of ZnO and

thus of the $O_2^{\bullet-}$ production. Due to the nanoscale sizes of ZnO and Ag particles, a larger interface is generated which favors the production of photoelectrons. Since t-BuOH used as an $^{\bullet}OH$ radical scavenger has only a weak detrimental role on the photocatalytic degradation, holes are likely to directly oxidize the pollutant rather the water molecules.

4. Conclusion

A new synthesis route for the preparation of small-sized ZnO NPs hybridized with Ag NPs was developed. Ag^+-doped LZHs were synthesized before photoreduction of Ag^+ ions into Ag(0) NPs. The LZHs matrix surrounding Ag particles maintains the nanosize (ca. 2.7 nm) and dispersibility of Ag particles. Next, the LZHs were converted into O-defective ZnO NPs by thermolysis at 300°C for 5 min. This fast and convenient synthesis strategy allows optimal dispersion of Ag NPs on the ZnO surface and does not require polymers or chelating agents to limit the growth of NPs. The photocatalytic activity under simulated sunlight irradiation of ZnO/Ag nanohybrids was evaluated for the degradation of RhB and RBBR dyes and of CIP. Results obtained show that the ZnO/Ag(3) catalyst exhibits the highest activity and that it is weakly sensitive to the pH of the solution from 5 to 11. The recyclability tests demonstrate a high stability in the photocatalytic performance. The excellent photocatalytic activity of the ZnO/Ag(3) nanohybrid originates from the good dispersion of Ag NPs, acting as electron sinks, at the surface of ZnO NP, which allows an efficient separation of photogenerated electron-hole pairs. The visible light absorption of the photocatalyst is also enhanced by the LSPR effect. This work demonstrates that Ag-doped LZHs are valuable precursors of ZnO/Ag hybrid photocatalysts and the synthetic strategy developed is anticipated to provide new avenues for the development of highly active nanosized photocatalysts for environmental and energy related applications.

CRediT authorship contribution statement

Mouna Ibn Mahrsi: Methodology, Investigation, Data curation, Writing – original draft. **Bilel Chouchene**: Methodology, Investigation, Data curation, Writing – original draft. **Thomas Gries**: Investigation, Data curation, Writing – original draft. **Vincent Carré**: Investigation, Data curation, Writing – original draft. **Emilien Girot**: Investigation, Data curation**. Ghouti Medjahdi**: Methodology, Investigation, Data curation. **Fadila Ayari**: Supervision, Funding

acquisition. **Lavinia Balan**: Investigation, Data curation, Writing – original draft. **Raphaël Schneider**: Supervision, Conceptualization, Writing – review & editing, Funding acquisition.

Declaration of Competing Interest

The authors declare that they have no known competing financial interests or personal relationships that could have appeared to influence the work reported in this paper.

Acknowledgments

This project has benefited from the expertise and the facilities of the Platform MACLE-CVL which was co-funded by the European Union and Centre-Val de Loire Region (FEDER).

Appendix A. Supplementary data

Supplementary material related to this article can be found, in the online version, at doi:https://

References

[1] Y. Boyjoo, H. Sun, J. Liu, V.K. Pareek, S. Wang, A review on photocatalysis for air treatment: From catalyst development to reactor design, Chem. Engineer. J. 310 (2017) 537-559.

[2] J.J. Rueda-Marquez, I. Levchuk, P. Fernandez Ibanez, M. Sillanpää, A critical review on application of photocatalysis for toxicity reduction of real wastewaters, J. Cleaner Prod. 258 (2020) 120694.

[3] S. Bai, N. Zhang, C. Gao, Y. Xiong, Defect engineering in photocatalytic materials, Nano Energy 53 (2018) 296-336.

[4] N. Fajrina, M. Tahir, A critical review in strategies to improve photocatalytic water splitting towards hydrogen production, Int. J. Hydrog. Energy 44 (2019) 540-577.

[5] J. Albero, Y. Peng, H. Garcia, Photocatalytic CO_2 reduction to C2+ products, ACS Catal. 10 (2020) 5734-5749.

[6] K.M. Lee, C.W. Lai, K.S. Ngai, J.C. Juan, Recent developments of zinc oxide based photocatalyst in water treatment technology: A review, Water Res. 88 (2016) 428-448.

[7] C.B. Ong, L.Y. Ng, A.W. Mohammad, A review of ZnO nanoparticles as solar photocatalysts: Synthesis, mechanisms and applications, Renewable Sustainable Energy Rev. 81 (2018) 536-551.

[8] X. Gu, C. Li, S. Yuan, M. Ma, Y. Qiang, J. Zhu, ZnO based heterojunctions and their application in environmental photocatalysis, Nanotechnology 27 (2016) 402001.

[9] S. Girish Kumar, K.S.K. Koteswara Rao, Zinc oxide based photocatalysis: tailoring surface-bulk structure and related interfacial charge carrier dynamics for better environmental applications, RSC Adv. 5 (2015) 3306-3351.

[10] S. Goktas, A. Goktas, A comparative study on recent progress in efficient ZnO based nanocomposite and heterojunction photocatalysts: A review, J. Alloys Compd. 863 (2021) 158734.

[11] L. He, S. Zhang, J. Zhang, G. Chen, S. Meng, Y. Fan, X. Zheng, S. Chen, Investigation on the mechanism and inner impetus of photogenerated charge transfer in WO_3/ZnO heterojunction photocatalysts, J. Phys. Chem. C 124 (2020) 27916-27929.

[12] M. Nemiwal, T.C. Zhang, D. Kumar, Recent progress in g-C_3N_4, TiO_2 and ZnO based photocatalysts for dye degradation: Strategies to improve photocatalytic activity, Sci. Total Environ. 767 (2021) 144896.

[13] M. Mrad, B. Chouchene, T. Ben Chaabane, T. Gries, G. Medjahdi, L. Balan, R. Schneider, Heterostructured photocatalysts associating ZnO nanorods and Ag-In-Zn-S quantum dots for the visible light-driven photocatalytic degradation of the acid orange 7 Dye, Catalysts 12 (2022) 1585.

[14] H. Moussa, B. Chouchene, T. Gries, L. Balan, K. Mozet, G. Medjahdi, R. Schneider, Growth of ZnO nanorods on graphitic carbon nitride gCN sheets for the preparation of photocatalysts with high visible-light activity, ChemCatChem 10 (2018) 4973-4983.

[15] H. Moussa, E. Girot, K. Mozet, H. Alem. G. Medjahdi, R. Schneider, ZnO rods/reduced graphene oxide composites prepared via a solvothermal reaction for efficient sunlight-driven photocatalysis, Appl. Catal. B: Environ. 185 (2016) 11-21.

[16] J. Meng, Q. Chen, J. Lu, H. Liu, Z-Scheme photocatalytic CO_2 reduction on a heterostructure of oxygen-defective ZnO/reduced graphene oxide/UiO-66-NH_2 under visible light, ACS Appl. Mater. Interfaces 11 (2019) 550-562.

[17] S. Prabhu, S. Megala, S. Harish, M. Navaneethan, P. Maadeswaran, S. Sohila, R. Ramesh, Enhanced photocatalytic activities of ZnO dumbbell/reduced graphene oxide

nanocomposites for degradation of organic pollutants via efficient charge separation pathway, Appl. Surf. Sci. 487 (2019) 1279-1288.

[18] B. Tatykayev, F. Donat, H. Alem, L. Balan, G. Medjahdi, B. Uralbekov, R. Schneider, Synthesis of core/Shell ZnO/rGO nanoparticles by calcination of ZIF-8/rGO composites and their photocatalytic activity, ACS Omega 2 (2017) 4946-4954.

[19] C. Feng, Z. Chen, J. Jing, J. Hou, The photocatalytic phenol degradation mechanism of Ag-modified ZnO nanorods, J. Mater. Chem. C 8 (2020) 3000-3009.

[20] Y. Liu, Q. Zhang, M. Xu, H. Yuan, Y. Chen, J. Zhang, K. Luo, J. Zhang, B. You, Novel and efficient synthesis of Ag-ZnO nanoparticles for the sunlight-induced photocatalytic degradation, Appl. Surf. Sci. 476 (2019) 632-640.

[21] L. Huang, D. Bao, X. Jiang, J. Li, L. Zhang, X. Sun, Fabrication of stable high-performance urchin-like CeO_2/ZnO@Au hierarchical heterojunction photocatalyst for water remediation, J. Colloid Interface Sci. 588 (2021) 713-724.

[22] R. Kavitha, S.G. Kumar, A review on plasmonic Au-ZnO heterojunction photocatalysts: Preparation, modifications and related charge carrier dynamics, Mater. Sci. Semicond. Process. 93 (2019) 59-91.

[23] C.A. Jaramillo-Paez, J.A. Navio, M.C. Hidalgo, M. Macias, ZnO and Pt-ZnO photocatalysts: Characterization and photocatalytic activity assessing by means of three substrates, Catal. Today 313 (2018) 12-19.

[24] C. Yu, K. Yang, Y. Xie, Q. Fan, J.C. Yu, Q. Shu, C. Wang, Novel hollow Pt-ZnO nanocomposite microspheres with hierarchical structure and enhanced photocatalytic activity and stability, Nanoscale 5 (2013) 2142-2151.

[25] Q. Zhang, J. Li, M. Xu, Ag-decorated ZnO-based nanocomposites for visible light-driven photocatalytic degradation: basic understanding and outlook, J. Phys. D: Appl. Phys. 55 (2022) 483001.

[26] S. Kuriakose, V. Choudhary, B. Satpati, S. Mohapatra, Facile synthesis of Ag–ZnO hybrid nanospindles for highly efficient photocatalytic degradation of methyl orange, Phys. Chem. Chem. Phys. 16 (2014) 17560-17568.

[27] S. Balachandran, S. Gopinathan Praveen, R. Velmuvugan, M. Swaminathan, Facile fabrication of highly efficient, reusable heterostructured Ag–ZnO–CdO and its twin applications of dye degradation under natural sunlight and self-cleaning, RSC Adv. 4 (2014) 4353-4362.

[28] E. Fardosi, H. Bahiraci, D. Ghanbari, Investigation the photocatalytic activity of $CoFe_2O_4$/ZnO and $CoFe_2O_4$/ZnO/Ag nanocomposites for purification of dye pollutants, Sep. Purif. Technol. 211 (2019) 35-39.

[29] S. Gea, S.A. Sibumorang, N. Pasaribu, A.F.R. Piliang, B. Attaurrazaq, R. Mustika Sari, K. Meldawati Pasaribu, S. Goutianos, Facile synthesis of ZnO–Ag nanocomposite supported by graphene oxide with stabilised band-gap and wider visible-light region for photocatalyst application, J. Mater. Res. Technol. 19 (2022) 2730-2741.

[30] Y. Liu, Q. Zhang, H. Yuan, K. Luo, J. Li, W. Hu, Z. Pan, M. Xu, S. Xu, I. Levchenko, K. Bazaka, Comparative study of photocatalysis and gas sensing of ZnO/Ag nanocomposites synthesized by one- and two-step polymer-network gel processes, J. Alloys Compd. 868 (2021) 158723.

[31] D. Tekin, T. Tekin, H. Kiziltas, Photocatalytic degradation kinetics of Orange G dye over ZnO and Ag/ZnO thin film catalysts, Sci. Rep. 9 (2019) 17544.

[32] U. Arif, F. Ali, A. Bahader, S. Ali, A. Zada, F. Raziq, Efficient visible light activities of Ag modified ZnO/g-C_3N_4 composite for CO_2 conversion, Inorg. Chem. Commun. 145 (2022) 109944.

[33] R. Pagano, A. Quarta, S. Pal, A. Licciulli, L. Valli, S. Bettini, Enhanced Solar-Driven Applications of ZnO@Ag Patchy Nanoparticles, J. Phys. Chem. C 121 (2017) 27199-27206.

[34] M. Kheirabadi, M. Samadi, E. Asadian, Y. Zhou, C. Dong, J. Zhang, A.Z. Moshfegh, Well-designed Ag/ZnO/3D graphene structure for dye removal: Adsorption, photocatalysis and physical separation capabilities, J. Colloid Interface Sci. 537 (2019) 66-78.

[35] M. Zare, K. Namralha, S. Alghassdi, Y.H. Eissa Mohammad, A. Hezam, M. Zara, Q.A. Drmosh, K. Byrappa, B.N. Chandrashekar, S. Ramakrishna, X. Zhang, Novel green biomimetic approach for synthesis of ZnO-Ag nanocomposite; antimicrobial activity against food-borne pathogen, biocompatibility and solar photocatalysis, Sci. Rep. 9 (2019) 8303.

[36] A.C. Trindade Cursino, J.E. Ferreira da Costa Gardolinski, F. Wypych, Intercalation of anionic organic ultraviolet ray absorbers into layered zinc hydroxide nitrate, J. Colloid Interface Sci. 347 (2010) 49-55.

[37] C. Yang, J. Yu, B. Huang, G. Miao, J. Xiao, Boosting deep desulfurization of heavy mercaptan using layered intercalated Zn-based hydroxide adsorbents, Sep. Purif. Technol. 307 (2023) 122860.

[38] T. Shinagawa, M. Watanabe, T. Mori, J. Tani, M. Chigane, M. Izaki, Oriented transformation from layered zinc hydroxides to nanoporous ZnO: A comparative study of different anion types, Inorg. Chem. 57 (2018) 13137-13149.

[39] W. Stählin, H.R. Oswald, The crystal structure of zinc hydroxide nitrate, $Zn_5(OH)_8(NO_3)_2.2H_2O$, Acta Cryst., Sect B: Struct. Crystallogr. Cryst. Chem. 26 (1970) 860-863.

[40] A. Gordeeva, Y.-J. Hou, I.Z. Jenei, P.H.B. Brant Carvalho, S.I. Simak, O. Andersson, U. Häussermann, Layered zinc hydroxide dihydrate, $Zn_5(OH)_{10}{\cdot}2H_2O$, from hydrothermal conversion of ε- $Zn(OH)_2$ at gigapascal pressures and its transformation to nanocrystalline ZnO, ACS Omega 5 (2020) 17617-17627.

[41] H. Nabipour, Y. Hu, Layered zinc hydroxide as vehicle for drug delivery systems: a critical review, J. Porous Mater. 29 (2022) 341-356.

[42] Z.P. Xu, J. Zhang, M.O. Adebajo, H. Zhang, C. Zhou, Catalytic applications of layered double hydroxides and derivatives, Appl. Clay. Sci. 53 (2011) 139-150.

[43] W. Ma, R. Ma, J. Liang, C. Wang, X. Liu, K. Zhou, T. Sasaki, Layered zinc hydroxide nanocones: synthesis, facile morphological and structural modification, and properties, Nanoscale 6 (2014) 13870-13875.

[44] P. Xu, L. Deng, Fabrication of orderly changed ZnO hierarchical structures by calcining different zinc precursors and morphology-depended photocatalytic property, Inorg. Chem. Comm. 137 (2022) 109215.

[45] S. Henriques Ferreira, M. Morais, D. Dunes, M. Joao Oliveira, A. Rovisco, A. Pimentel, H. Aguas, E. Fortunato, R. Martins, High UV and sunlight photocatalytic performance of porous ZnO nanostructures synthesized by a facile and fast microwave hydrothermal method, Materials 14 (2021) 2385.

[46] N. Mukwevho, R. Gusain, E. Fosso-Kankeu, N. Kumar, F. Waanders, S. Sinha Ray, Removal of naphthalene from simulated wastewater through adsorption-photodegradation by ZnO/Ag/GO nanocomposite. J. Ind. Eng. Chem. 81 (2020) 393-404.

[47] Z. Ming, C. Jiehu, Z. Jie, P. Li, X. Du, C. Li, TEA-assisted hydro-thermal synthesis of layered Zn hydroxide nitrate adsorbent and its rapid adsorption for MO, Inorg. Nano-Met. Chem. 52 (2022) 204-212.

[48] Y. Zheng, H. Deng, H. Feng, G. Luo, R. Tu, L. Zhang, Triethanolamine-assisted synthesis of NiFe layered double hydroxide ultrathin nanosheets for efficient oxygen evolution reaction, J. Colloid Interface Sci. 629 (2023) 610-619.

[49] A.C. Trindade Cursino, J.E. Ferreira da Costa Gardolinski, F. Wypych, Intercalation of anionic organic ultraviolet ray absorbers into layered zinc hydroxide nitrate. J. Colloid Interface Sci. 347 (2010) 49-55.

[50] L. Wu, Y. Wu, L. Wei, Preparation of ZnO nanorods and optical characterizations, Phys. E: Low-Dimens. Syst. Nanostructures 28 (2005) 76-82.

[51] W. Stählin, H. R. Oswald, The crystal structure of zinc hydroxide nitrate, $Zn_5(OH)_8(NO_3)_2.2H_2O$, Acta Cryst. 26B (1970) 860-863.

[52] J. Fan, R. Freer, The roles played by Ag and Al dopants in controlling the electrical properties of ZnO varistors, J. Appl. Phys. 77 (1995) 4795.

[53] C.L. Du, Z.B. Gu, M.H. Lu, J. Wang, S.T. Zhang, J. Zhao, G.X. Cheng, H. Heng, Y.F. Chen, Raman spectroscopy of (Mn, Co)-codoped ZnO films, J. Appl. Phys. 99 (2006) 123515.

[54] S.S. Patil, M.G. Mali, M.S. Tamboli, D.R. Patil, M.V. Kulkarni, H. Yoon, H. Kim, S.S. Al-Deyab, S.S. Yoon, S.S. Kolekar, B.B. Kale, Green approach for hierarchical nanostructured Ag-ZnO and their photocatalytic performance under sunlight, Catal. Today 260 (2016) 126-134.

[55] Q. Zhang, G. Xie, M. Xu, Y. Su, H. Tai, H. Du, Y. Jiang, Visible light-assisted room temperature gas sensing with ZnO-Ag heterostructure nanoparticles, Sens. Actuators B Chem. 259 (2017) 269-281.

[56] A.M. Jones, S. Garg, D. He, A.N. Pham, T.D. Waits, Superoxide-mediated formation and charging of silver nanoparticles, Environ. Sci. Technol. 45 (2011) 1428-1434.

[57] C. Chen, Y. Zheng, Y. Zhan, X. Lin, Q. Zheng, K. Wei, Enhanced Raman scattering and photocatalytic activity of Ag/ZnO heterojunction nanocrystals, Dalton Trans. 40 (2011) 9566-9570.

[58] S. Livic, P. Christopher, D.B. Ingram, Plasmonic-metal nanostructures for efficient conversion of solar to chemical energy, Nat. Mater. 10 (2011) 911-921.

[59] R. Raji a, K.S. Sibi b, K.G. Gopchandrana, ZnO:Ag nanorods as efficient photocatalysts: Sunlight driven photocatalytic degradation of sulforhodamine B, Appl. Surf. Sci. 427 (2018) 863–875.

[60] B. Sarma, B.K. Sarma, Fabrication of Ag/ZnO heterostructure and the role of surface coverage of ZnO microrods by Ag nanoparticles on the photophysical and photocatalytic properties of the metal-semiconductor system, Appl. Surf. Sci. 410 (2017) 557-565.

[61] L. Zhang, L. Yin, C. Wang, N. Iun, Y. Qi, D. Xiang, Origin of visible photoluminescence of ZnO quantum dots: defect-dependent and size-dependent, J. Phys. Chem. C 114 (2010) 9651-9658.

[62] H.-Y. Shi, B. Deng, S.-L. Zhong, L. Wang, A.-W. Xu, Synthesis of zinc oxide nanoparticles with strong, tunable and stable visible light emission by solid-state transformation of Zn(II)–organic coordination polymers, J. Mater. Chem. 21 (2011) 12309-12315.

[63] F. Mohd Omar, H. Abdul Aziz, S. Stoll, Stability of ZnO nanoparticles in solution. Influence of pH, dissolution, aggregation and disaggregation effects, J. Colloid Sci. Biotechnol. 3 (2014) 75-84.

[64] I. Kazeminezhad, A. Sadollahkhani, Influence of pH on the photocatalytic activity of ZnO nanoparticles, J. Mater. Sci. : Mater. Electron. 27 (2016) 4206-4215.

[65] A. Kutuzova, T. Dontsova, W. Kwapinski, Application of TiO_2-based photocatalysts to antibiotics degradation: Cases of sulfamethoxazole, Trimethoprim and Ciprofloxacin, Catalysts 11 (2021) 728.

[66] Y. Xu, M. A. A. Schoonen, The absolute energy positions of conduction and valence bands of selected semiconducting minerals, Am. Mineral. 85 (2000) 543-556.

[67] Q. Deng, X. Duan, D.H.L. Ng, H. Tang, Y. Yang, M. Kong, Z. Wu, W. Cai, G. Wang, Ag nanoparticle decorated nanoporous ZnO microrods and their enhanced photocatalytic activities, ACS Appl. Mater. Interfaces 4 (2012) 6030-6037.

[68] F. Yan, Y. Wang, J. Zhang, Z. Lin, J. Zheng, F. Huang, Schottky or ohmic metal–semiconductor contact: Influence on photocatalytic efficiency of Ag/ZnO and Pt/ZnO model systems, ChemSusChem 7 (2014) 101-104.